Preprint Cambridge Centre for Computational Chemical Engineering ISSN 1473 – 4273

Population balance modelling of TiO_2 synthesis in a stagnation flame

Manoel Manuputty [1], Jethro Akroyd [1], Sebastian Mosbach [1], Markus Kraft [1,2]

released: 1 July 2016

[1] Department of Chemical Engineering
and Biotechnology
University of Cambridge
New Museums Site
Pembroke Street
Cambridge, CB2 3RA
United Kingdom
E-mail: mk306@cam.ac.uk

[2] School of Chemical and
Biomedical Engineering
Nanyang Technological University
62 Nanyang Drive
637459
Singapore

Preprint No. 169

Keywords: TiO_2, TTIP, population balance, stagnation, flame

Edited by
Computational Modelling Group
Department of Chemical Engineering and Biotechnology
University of Cambridge
New Museums Site
Pembroke Street
Cambridge CB2 3RA
United Kingdom

Fax: + 44 (0)1223 334796
E-Mail: c4e@cam.ac.uk
World Wide Web: http://como.ceb.cam.ac.uk/

Abstract

The stagnation flame synthesis of titanium dioxide nanoparticles from titanium tetraisopropoxide (TTIP) is modelled using a population balance model based on a simple one-step decomposition mechanism and one-dimensional stagnation flow. The population balance model includes nucleation, surface growth and coagulation processes and is closed using the method of moment with interpolative closure (MoMIC). The model shows excellent agreement with experimental data for different TTIP loadings in a flame stabilized on a rotating surface (FSRS). The particle size was observed to be sensitive to the sampling location in the modelled flame, offering a plausible explanation for the discrepancy between experimental particle sizes measured via aerosol sampling versus transmission electron microscopy (TEM) of samples collected using grid insertion. The sensitivity to the sampling location is found to increase with increasing precursor loading and stagnation temperature. Lastly, the effect of surface growth is evaluated by comparing the result with an alternative particle model. It is found that surface growth plays an important role in the initial stage of particle growth which results in severe under-prediction of particle size if neglected.

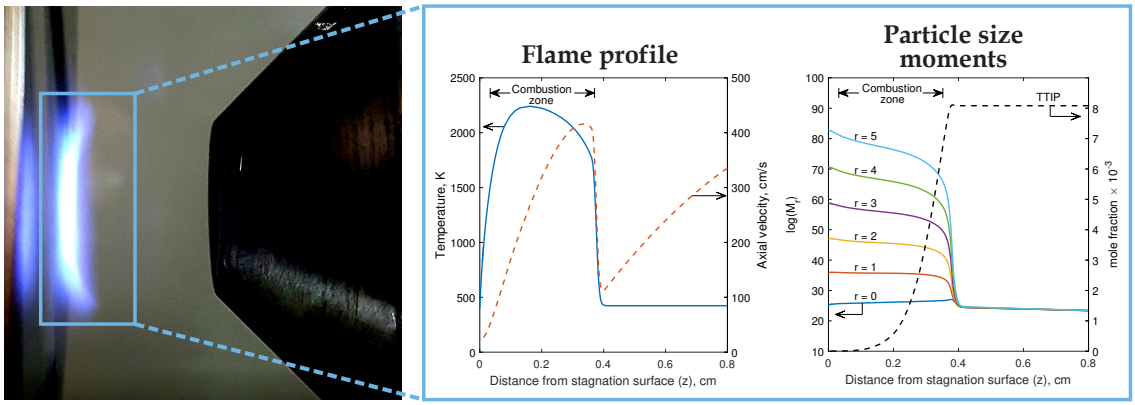

Highlights

- Particle population balance model of TiO_2 synthesis from titanium tetraisopropoxide (TTIP) is solved using method of moments with interpolative closure (MoMIC).
- A simple reaction model for TTIP decomposition is sufficient to simulate the particle sizes in a flame stabilized on rotating surface (FSRS) experiment.
- Particle size is found to be sensitive to the sampling location near the stagnation surface, especially for high TTIP loading and stagnation temperature.
- Surface growth plays an important role in the initial growth stage of particles.

Contents

1 Introduction

Titanium dioxide (TiO_2) is a material with wide industrial applications. It exists mainly as anatase and rutile polymorphs. Anatase is used in photocatalysis and photovoltaic applications due to its photoactivity while rutile is mainly used in white pigment due to its high refractive index. Pigment is the single greatest use of titanium worldwide with annual global production of 7.2 million tonnes of TiO_2 in 2015 [40]. For many applications, including pigments, the ability to control the nanoparticle properties, for example size distribution and crystallinity, is critical to the performance of the material.

Despite its commercial importance, a complete understanding of the formation of titanium dioxide, also known as titania, is still lacking. One of the main manufacturing processes is the chloride process with titanium tetrachloride ($TiCl_4$) as the presursor. The main difficulty lies in the fact that the chloride process involves harsh reaction conditions at high temperature which limit the ability to perform experimental analysis. The experimental studies are further complicated by the inherent challenges in nanoscale characterization. Computational modeling offers attractive capabilities to investigate such systems and combined with well designed experimental work, to provide insights into the particle formation [20, 30–32, 37, 45, 46].

Another common precursor of TiO_2 is titanium tetraisopropxide (TTIP). TTIP is often preferred as an alternative to $TiCl_4$ for lab-scale studies because it is more stable and easier to handle. A number of works have combined experimental studies and computational tool, in particular population balance modelling, in order to investigate how the various processes like nucleation, surface growth, coagulation and coalescence affect the particle properties in TTIP-TiO_2 system [38, 39, 48, 51].

Tsantilis et al. [39] solved a population balance model with different reaction models and compared the results with experimental data from a premixed methane-oxygen flat flame. They found that the reaction model which includes surface growth is most consistent with the experimental data, especially near the burner face (< 1 cm) and so concluded that surface reaction is an important growth mechanism. However, they observed that further away from the burner, neglecting surface growth also yielded a good agreement with experimental data because coagulation was already dominant. This suggests that surface growth is dominant in the early stage of particle formation while coagulation in later stages.

The importance of coagulation was also observed by Zhao et al. [51] using a burner-stabilized stagnation flame (BSSF) with embedded aerosol sampling probe. The experimental data was compared with a population balance model solved with a sectional method. They observed that the high residence time in the experiment resulted in large aggregate structure with relatively broad particle size distribution. In another study, Yu et al. [48] compared the experimental data from a diffusion flame reactor and the population balance model solved with a quadrature method of moments (QMoM). They showed that higher particle residence time in the high temperature zone led to formation of irregular agglomerates.

Tsantilis and Pratsinis [38] showed theoretically that limiting particle residence time (or freezing the particle growth) is necessary in order to produce particles with narrow size

distribution. Such operating conditions are achieved by either quenching in critical flow nozzles [44] or using impinging jets on stagnation plate [22, 26, 35].

Tolmachoff et al. [35] introduced a flame stabilized on rotating surface (FSRS) technique to produce TiO_2 nanoparticles with narrow size distribution. In this method, a TTIP-doped premixed $C_2H_4/O_2/Ar$ jet impinges on a rotating stagnation surface which acts as a substrate holder. A flat flame is formed and stabilized very close to the stagnation surface due to the high jet velocity, confining the high temperature zone within 3-4 mm from the surface. The surface is cooled by forced convection, resulting in a high temperature gradient which facilitates particle deposition by thermophoresis. As a result of the small combustion zone very near to the stagnation surface, particle growth is quenched at early stage leading to particle size distribution narrower than the self-preserving distribution [21]. More importantly, the particle properties including size distribution and crystallinity were shown to be able to be controlled by varying the experimental conditions including stagnation temperature and precursor loading. Korobeinichev et al. [19] also used a similar technique to produce crystalline TiO_2 with narrow size distribution from a TTIP-doped $H_2/O_2/Ar$ flame.

In addition to the ability to produce crystalline nanoparticles or films for various applications [26, 36], the features of FSRS offer the ability to study early particle formation of TiO_2 from TTIP. This could be used to improve our understanding of chemical decomposition of TTIP and the reactions leading to the formation of TiO_2. It also provides data against which to assess the detailed mechanisms, for example those proposed by Buerger et al. [7] and Shmakov et al. [33].

Previous studies have modelled similar flames without particles [19, 22, 35] while others introduced the particle formation in post-processing [51]. Modak et al. [24] attempted to couple the gas-phase and particle population balance using a BSSF configuration and sectional method but ignored the effect of surface growth which has been shown to be critical by earlier studies.

The purpose of this paper is to implement a population balance model by employing a simple reaction model available in literature and to demonstrate the ability to model TiO_2 formation from TTIP in FSRS. The predicted results are compared with experimental data obtained from Tolmachoff et al. [35]. This work aims to investigate the effects of varying important process parameters, including precursor loading and stagnation temperature, and to explain experimentally observed trends of particle size in terms of relative rates of the particle processes modelled. In particular, we aim to understand the role of surface growth on particle growth in the FSRS experiment.

2 Model description

2.1 Flow model

The flow in the burner was assumed to be an axisymmetric stagnation flow. It was modelled using pseudo one-dimensional approximation, illustrated in Figure 1, by introducing a streamfunction of the form

$$\Psi(z,r) = r^2 U(z),$$

where z is the axial distance from the nozzle, r is the radial distance from the burner centerline, and $U(z)$ is the axial component of the streamfunction. The axial velocity, u_z, and radial velocity, u_r, are given by

$$u_z = \frac{2U(z)}{\rho}$$
$$u_r = -\frac{r}{\rho}\frac{\mathrm{d}U(z)}{\mathrm{d}z},$$

where ρ is the gas mixture density.

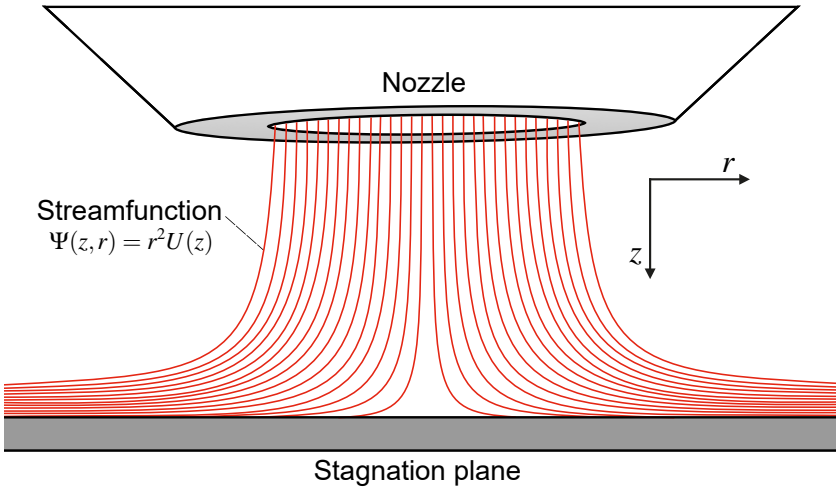

Figure 1: *Diagram of a one-dimensional stagnation flow with streamlines shown in red.*

By introducing the streamfunction assumption, the Navier-Stokes equations are reduced to a set of one-dimensional ordinary differential equations [more on derivation in 18],

$$\frac{\mathrm{d}\Lambda}{\mathrm{d}z} = 0 \tag{1}$$

$$\Lambda - 2\frac{\mathrm{d}}{\mathrm{d}z}\left(\frac{UG}{\rho}\right) + \frac{3G^2}{\rho} + \frac{\mathrm{d}}{\mathrm{d}z}\left[\mu\frac{\mathrm{d}}{\mathrm{d}z}\left(\frac{G}{\rho}\right)\right] = 0, \tag{2}$$

where Λ is the radial pressure-gradient eigenvalue, G is $\mathrm{d}U/\mathrm{d}z$ and μ is the gas mixture viscosity. Equations 1 and 2 are the eigenvalue and the momentum equations for one-dimensional stagnation flow, respectively. Next, assuming the temperature, T, and the

species mole fractions, Y_k, are radially independent, the additional governing equations for T and Y_k are given as

$$2U\frac{\mathrm{d}T}{\mathrm{d}z} - \frac{1}{c_p}\frac{\mathrm{d}}{\mathrm{d}z}\left(\lambda\frac{\mathrm{d}T}{\mathrm{d}z}\right) + \frac{\rho}{c_p}\sum_{k=1}^{K} Y_k c_{p,k} V_k \frac{\mathrm{d}T}{\mathrm{d}z} + \frac{1}{c_p}\sum_{k=1}^{K} h_k \dot{\omega}_k + \frac{1}{c_p}\dot{Q}_{\mathrm{rad}} = 0 \tag{3}$$

$$2U\frac{\mathrm{d}Y_k}{\mathrm{d}z} + \frac{\mathrm{d}}{\mathrm{d}z}(\rho Y_k V_k) - W_k \dot{\omega}_k = 0 \quad (k = 1, K), \tag{4}$$

where c_p is the mixture specific heat, λ is the mixture thermal conductivity, $\dot{Q}_{\mathrm{rad}}$ is the gas radiation term in the optically-thin limit [34], K is the number of gas-phase species, Y_k, $c_{p,k}$, h_k, $\dot{\omega}_k$, V_k and W_k are the mole fraction, the specific heat, the molar enthalpy, the molar production rate, the multicomponent diffusion velocity, and the molar mass of species k, respectively.

This model has been used to simulate various combustion systems successfully before where the simplified flow reduces computational power required. This is an attractive benefit for cases where coupling with complex and computationally expensive reacting systems is necessary [8, 47].

2.2 Gas phase chemistry

The combustion chemistry and transport data of the gas species were described by the USC-Mech II hydrocarbon kinetic model which includes 111 species and 784 reactions [42]. TTIP was added as an extra species. TTIP thermodynamic data was obtained from first-principle calculations by Buerger et al. [6] while the transport data was estimated from the transport data for large hydrocarbons [9]. The approximation of the transport data was deemed acceptable given the relatively low loading of TTIP simulated in this work. The mechanism, thermodynamic, and transport data used in this study is included in the supplementary material.

2.3 Particle model

2.3.1 Reaction model

In this work, the simple one-step reaction proposed by Okuyama et al. [27] was used to describe the overall rate of TTIP consumption with first order reaction rate constant given by

$$k_1 = 3.96 \times 10^5 \exp\left(\frac{-8479.7\ \mathrm{K}}{T}\right)\ \mathrm{s}^{-1}. \tag{5}$$

The overall reaction was assumed to include both gas-phase decomposition and surface reaction of TTIP. The surface reaction rate was described by the first-order rate model proposed by Battiston et al. [3] with rate constant derived by Tsantilis et al. [39],

$$k_2 = 1 \times 10^{11} \exp\left(\frac{-15155.16\ \mathrm{K}}{T}\right)\ \mathrm{cm/s}. \tag{6}$$

The rate of the gas-phase decomposition of TTIP was calculated from the difference between the overall and surface reaction rates. When the surface reaction rate exceeds the overall rate, the gas-phase decomposition rate was turned to zero and the surface reaction rate was calculated from the overall rate instead. In summary, the chemical reactions modelled leading to TiO_2 formation are

$$\mathrm{Ti(OC_3H_7)_{4(g)}} \xrightarrow{k_g} \mathrm{TiO_{2(s)} + 4C_3H_{6(g)} + 2H_2O_{(g)}} \tag{7}$$

$$\mathrm{Ti(OC_3H_7)_{4(g)} + (TiO_2)_{i-1(s)}} \xrightarrow{k_s} \mathrm{(TiO_2)_{i(s)} + 4C_3H_{6(g)} + 2H_2O_{(g)}}, \tag{8}$$

with the gas-phase reaction rate constant, k_g, and the surface reaction rate constant, k_s, given by

$$k_g = \begin{cases} k_1 - Ak_2 & \text{for } k_1 \geq Ak_2 \\ 0 & \text{for } k_1 < Ak_2 \end{cases} \tag{9}$$

$$k_s = \begin{cases} k_2 & \text{for } k_1 \geq Ak_2 \\ k_1/A & \text{for } k_1 < Ak_2, \end{cases} \tag{10}$$

where A is the total surface area of the particles per unit volume. Considering the relatively low loading of TTIP simulated in this study, these reactions were neglected from temperature source term calculation in Equation 3.

A similar model was used by Tsantilis et al. [39] and was shown to result in excellent agreement with experimental data. In addition, this reaction rate model was shown to sufficiently describe the overall TTIP consumption in a H_2/O_2 stagnation flame experiment conducted by Korobeinichev et al. [19]. A more recent study of TTIP decomposition in an aerosol reactor [43] also supported the first-order overall rate as proposed by Okuyama et al. [27] for high temperature conditions.

2.3.2 Population balance model

The particle population was described by the number density moments of the size distribution, M_r, which are defined as

$$M_r = \sum_{i=1}^{\infty} i^r N_i \tag{11}$$

$$\mu_r = \frac{M_r}{M_0}, \tag{12}$$

where r is the order of the moment, N_i is the number density of particles with i TiO_2 monomers, and μ_r are the reduced moments. The method of moments has been widely used to solve population balance models in areas such as aerosol science, materials science, and cell biology. Hulburt and Katz [17] were one of the first to develop the method of moments to model particles in inhomogeneous flow in 1964. Frenklach and Harris [12] later extended the method to use interpolation to provide closures in the method of moments with interpolative closure (MoMIC), used in this work.

While complete reconstruction of the full particle size distribution requires the knowledge of all moments, a number of relevant properties such as number density, area density, mass density, and average diameter, can be inferred from the first few moments alone. These population properties are given by

$$\text{Number density} = M_0 \tag{13}$$

$$\text{Area density} = A_1 M_{2/3} \tag{14}$$

$$\text{Mass density} = m_1 M_1 \tag{15}$$

$$\text{Average diameter} = d_1 \frac{M_{1/3}}{M_0}, \tag{16}$$

where A_1, m_1 and d_1 are the surface area, the mass, and the diameter of a single TiO_2 monomer, respectively. The surface area and diameter were calculated from m_1 and the bulk density of rutile.

The accuracy of the interpolation used in MoMIC depends on the number of moments. Six moments are normally used, in this case the zeroth to fifth order moments. Thus, the particle population is tracked by only six moment equations. This provides computational economy without having to make any prior assumptions about the distribution.

The spherical particle model, which assumes instantaneous coalescence, is imposed by the choice of the method of moments model. However, it is noted that this assumption is consistent with the high resolution TEM (HRTEM) observations in Nikraz and Wang [26] where the particles were found to be mostly spherical with occasional sintered necks. This is due to the fact that the temperature in the combustion zone is much higher than the melting point of bulk TiO_2 ($\sim$1900 K) which leads to rapid sintering. In cases where particles form aggregate structure, a more detailed particle model which includes aggregation and sintering is required [15, 23, 25].

The population balance was coupled to the flow and gas-phase chemistry through transport equations describing convection, thermal diffusion, size-dependent molecular diffusion and moment source terms. The transport equation for the r^{th}-moment is given in logarithmic form as

$$2U\frac{\mathrm{d}}{\mathrm{d}z}\left(\frac{1}{\rho}\right) + \frac{2U}{\rho}\frac{\mathrm{d}\log M_r}{\mathrm{d}z} + \frac{2}{\rho}\frac{\mathrm{d}U}{\mathrm{d}z} - \frac{2G}{\rho} + v_{T,z}\frac{\mathrm{d}\log M_r}{\mathrm{d}z} + \frac{\mathrm{d}v_{T,z}}{\mathrm{d}z} - \frac{1}{M_r}\frac{\mathrm{d}}{\mathrm{d}z}\left[\rho D_{p,1}\frac{\mathrm{d}}{\mathrm{d}z}\left(\frac{M_{r-2/3}}{\rho}\right)\right] - \frac{\dot{M}_r}{M_r} = 0, \tag{17}$$

where $D_{p,1}$ is the Brownian diffusion coefficient of TiO_2 monomer, $v_{T,z}$ is the thermophoretic velocity, $\dot{M}_r$ is the moment source terms. The formulations for $D_{p,1}$ and $v_{T,z}$ [41] are given as

$$D_{p,1} = \frac{3}{2\rho}\left(1 + \frac{\pi\alpha_T}{8}\right)^{-1}\sqrt{\frac{\bar{W}k_{\mathrm{B}}T}{2\pi N_{\mathrm{A}}}}\left(\frac{1}{d_1^2}\right)$$

$$v_{T,z} = -\frac{3}{4}\left(1 + \frac{\pi\alpha_T}{8}\right)^{-1}\frac{\mu}{\rho}\frac{\mathrm{d}\log T}{\mathrm{d}z},$$

where α_T is the thermal accommodation factor which represents the equilibrium fraction of gas molecules that leave the particle surface and is usually about 0.9 [13], $\bar{W}$ is the average molar mass of the gas mixture, k_B is the Boltzmann constant and N_A is the Avogadro number.

The moment source terms, $\dot{M}_r$, describe the evolution of the moments according to particle processes, including inception, surface growth, and coagulation,

$$\dot{M}_r = \dot{M}_r^{\mathrm{in}} + \dot{M}_r^{\mathrm{sg}} + \dot{M}_r^{\mathrm{coag}}, \tag{18}$$

where $\dot{M}_r^{\mathrm{in}}$ and $\dot{M}_r^{\mathrm{sg}}$ represent the moment source terms due to inception and surface growth described in the reaction model, respectively. With the reaction model described in section 2.3.1, these terms are given as

$$\dot{M}_r^{\mathrm{in}} = k_g C_{\mathrm{TTIP}} N_\mathrm{A} \qquad \text{for } r \geq 0 \tag{19}$$

$$\dot{M}_r^{\mathrm{sg}} = \begin{cases} 0 & \text{for } r = 0 \\ k_s A_1 C_{\mathrm{TTIP}} N_\mathrm{A} \displaystyle\sum_{k=0}^{r-1} \binom{r}{k} \mu_{k+\frac{2}{3}} M_0 & \text{for } r \geq 1, \end{cases} \tag{20}$$

where C_{TTIP} is the TTIP molar concentration in the gas-phase. It is noted that the moment source term due to inception is independent of the moment order, r, because the smallest particle in the population is assumed to have $i = 1$ (e.g. a TiO_2 monomer).

The moment source term due to coagulation, $\dot{M}_r^{\mathrm{coag}}$, follows the formulation proposed by Pratsinis [28],

$$\dot{M}_r^{\mathrm{coag}} = \begin{cases} \dfrac{G_r^c G_r^f}{G_r^c + G_r^f} & \text{for } r \neq 1 \\ 0 & \text{for } r = 1, \end{cases} \tag{21}$$

where G_c and G_f are the moment source terms due to coagulation in the continuum and free-molecular regimes, respectively. The coagulation source term in the continuum regime for spherical particles is given as [derivation in 11]

$$G_r^c = \begin{cases} -K_c \left(1 + \mu_{\frac{1}{3}} \mu_{-\frac{1}{3}} + K_c' [\mu_{-\frac{1}{3}} + \mu_{\frac{1}{3}} \mu_{-\frac{2}{3}}]\right) M_0^2 & \text{for } r = 0 \\ 0 & \text{for } r = 1 \\ \dfrac{1}{2} K_c \displaystyle\sum_{k=1}^{r-1} \binom{r}{k} \left(\beta_1^c(r,k) + K_c' \beta_2^c(r,k)\right) M_0^2 & \text{for } r \geq 2 \end{cases} \tag{22}$$

$$K_c = \frac{2 k_\mathrm{B} T}{3\mu}$$

$$K_c' = 2.514 \lambda_l \left(\frac{\pi \rho_{\mathrm{TiO_2}}}{6 m_1}\right)^{\frac{1}{3}}$$

$$\beta_1^c(r,k) = \mu_{k+\frac{1}{3}} \mu_{r-k-\frac{1}{3}} + 2\mu_k \mu_{r-k} + \mu_{k-\frac{1}{3}} \mu_{r-k+\frac{1}{3}}$$

$$\beta_2^c(r,k) = \mu_{k+\frac{1}{3}} \mu_{r-k-\frac{2}{3}} + \mu_k \mu_{r-k-\frac{1}{3}} + \mu_{k-\frac{1}{3}} \mu_{r-k} + \mu_{k-\frac{2}{3}} \mu_{r-k+\frac{1}{3}},$$

where λ_l is the mean free path and ρ_{TiO_2} is the bulk density of rutile titania.

The coagulation source term in the free-moleculer regime for spherical particles is given as [derivation in 11]

$$G_r^f = \begin{cases} -\frac{1}{2} K_f \left({}^{\frac{1}{2}}f_{0,0} \right) M_0^2 & \text{for } r = 0 \\ 0 & \text{for } r = 1 \\ \frac{1}{2} K_f \sum_{k=1}^{r-1} \binom{r}{k} \left({}^{\frac{1}{2}}f_{k,r-k} \right) M_0^2 & \text{for } r \geq 2 \end{cases} \tag{23}$$

$$K_f = \varepsilon_{i,j} \left(\frac{6 k_\mathrm{B} T}{\rho_{\mathrm{TiO}_2}} \right)^{\frac{1}{2}} \left(\frac{3 m_1}{4 \pi \rho_{\mathrm{TiO}_2}} \right)^{\frac{1}{6}}$$

$${}^{l}f_{x,y} = \sum_{i=1}^{\infty} \sum_{j=1}^{\infty} \frac{i^x j^y}{\sqrt{ij}} (i+j)^l \left(i^{\frac{1}{3}} + j^{\frac{1}{3}} \right)^2 \frac{N_i N_j}{M_0^2},$$

where $\varepsilon_{i,j}$ is the size-dependent collision enhancement factor due to attractive or repulsive inter-particle forces. In this case, a constant multiplier, ε, is assumed to replace the size-dependent enhancement factor as normally used for soot coagulation [16]. The enhancement factor used in this study is 2.64 which was calculated by Zhang et al. [49] considering both van der Waals and dipole-dipole interaction of TiO_2 particles in free-molecular regime at high temperature. The enhancement factor used for soot is only slightly lower, 2.2 [16].

Finally, closures for the fractional moment terms were obtained from Lagrange interpolation (or extrapolation in case of negative order moments) among the known values of whole order moments as prescribed by Frenklach et al. [11],

$$\log \mu_p = L_p \left(\log \mu_0, \log \mu_1, ..., \log \mu_{r_{\max}} \right) \qquad \text{for } p > 0 \tag{24}$$

$$\log \mu_p = L_p \left(\log \mu_0, \log \mu_1, \log \mu_2 \right) \qquad \text{for } p < 0. \tag{25}$$

The function ${}^{\frac{1}{2}}f_{x,y}$ was estimated by logarithmic Lagrange interpolation between evaluations of the grid function,

$${}^{m}f_{x,y} = \sum_{k=0}^{m} \binom{m}{k} \left(\mu_{k+x+\frac{1}{6}} \mu_{m+y-k-\frac{1}{2}} + 2\mu_{k+x-\frac{1}{6}} \mu_{m+y-k-\frac{1}{6}} + \mu_{k+x-\frac{1}{2}} \mu_{m+y-k+\frac{1}{6}} \right),$$

for $m \in \mathbb{N}_0$, using the parameterisation

$$\begin{aligned} m &= 0, ..., n-1 \\ n &= \min(4, U - \max(x,y)) \quad \text{with } U \in \{3, ..., 6\}, \end{aligned}$$

where U is the number of moments evolution equations being solved, six in this case, such that $r = 0, ..., U-1$ [1].

2.4 Boundary conditions

The set of governing equations in 1–4 and 17 represent a fully-coupled system of fluid flow, gas-phase chemistry and particles. The equations were solved as a boundary value problem by specifying a set of boundary conditions at the burner nozzle and stagnation plane.

The boundary conditions at $z = 0$ (nozzle) are given as

$$U(0) = \frac{\rho_0 u_0}{2} \tag{26}$$

$$G(0) = 0 \tag{27}$$

$$T(0) = T_0 \tag{28}$$

$$\rho(0) Y_k(0) V_k(0) = \rho_0 u_0 (Y_{k,0} - Y_k(0)) \qquad \text{for } k = 1, ..., K \tag{29}$$

$$\log M_r(0) = 0 \qquad \text{for } r = 0, ..., 5, \tag{30}$$

where u_0, ρ_0, T_0, and $Y_{k,0}$ are the exit velocity, density, temperature, and mole fraction of species k of the gas mixture in the nozzle, respectively. The formulation of the boundary condition of the species mole fraction, Y_k, allows for back-diffusion into the nozzle which leads to $Y_{k,0} \neq Y_k(0)$. As the particles were supposed to be non-existent in the initial gas mixture in the nozzle, M_r should be zero. However, as the moments were tracked in log-space, $\log M_r$, this boundary condition was not feasible. Instead, $\log M_r(0) = 0$ was used, corresponding to negligible but non-zero particle concentration. This choice was justified by the fact that the high temperature region is located far from the nozzle, which results in insensitivity to the choice of $\log M_r(0)$.

The boundary conditions at $z = L$ (stagnation plane) are given as

$$U(L) = 0 \tag{31}$$

$$G(L) = 0 \tag{32}$$

$$T(L) = T_s \tag{33}$$

$$\rho(L) Y_k(L) V_k(L) = 0 \qquad \text{for } k = 1, ..., K \tag{34}$$

$$\frac{\mathrm{d} \log M_r(L)}{\mathrm{d}z} = 0 \qquad \text{for } r = 0, ..., 5, \tag{35}$$

where T_s is the stagnation temperature.

3 Computational details

All of the simulations presented in this work were performed using the *k*inetics® software package [10]. The boundary-value problem, described in section 2.4, was solved using a damped Newton search algorithm to obtain the steady-state solution [similar to 14].

The convergence criterion was specified by setting a tolerance level which controls the grid refinement to resolve the regions with large magnitudes of the gradient and curvature of the dependent variables. Using the solution-adapted grid refinement, convergence was achieved with 250–300 grid points for the nozzle-stagnation plate separation distance,

$H = 1.27$ cm, and 400–450 grid points for $H = 3.4$ cm. By way of comparison, Modak et al. [24] used only around 200 grid points for $H = 3.4$ cm with a similar flame.

The experimental conditions in Tolmachoff et al. [35] were used in all simulations in this work except where otherwise stated. The initial molar composition of the gas mixture was 3.96% C_2H_4, 26.53% O_2, and 69.51% Ar (corresponding to an equivalence ratio of $\phi = 0.45$) while TTIP loading was varied from 10–2000 ppm. The other boundary conditions were specified as

$$u_0 = 429 \text{ cm/s}$$
$$T_0 = 423.15 \text{ K}$$
$$T_s = 400 - 1600 \text{ K}.$$

The gas radiation model for temperature correction, under the assumption of optically-thin flames, including the radiation from H_2O, CO_2, CO, and CH_4 [2] was used for all simulations presented in this work.

4 Results and discussion

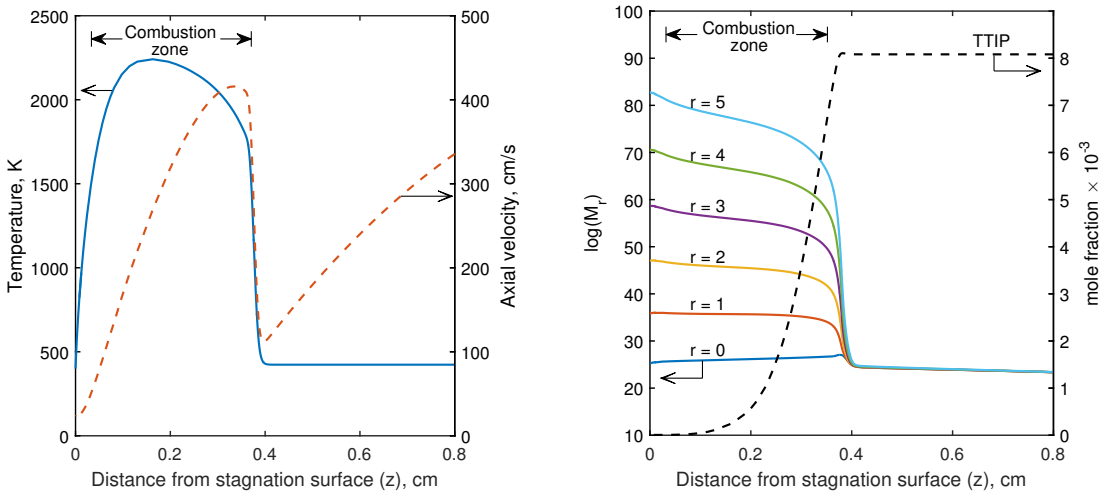

(a) Temperature and axial velocity profiles.

(b) Particle moments, M_r, evolution (r = moments order) and TTIP mole fraction profiles.

Figure 2: *Results of 1000 ppm TTIP loading simulation showing temperature, velocity, TTIP mole fraction, and moments profiles. The high temperature region, or combustion zone, is shown.*

Figure 2 shows the steady-state flame solution for 1070 ppm TTIP loading. The results are plotted with $z = 0$ being the location of the stagnation surface (as for all figures in this work).

Fig. 2(a) shows the simulated temperature profile. Initially, the temperature is constant, equal to the gas temperature in the nozzle. At $z = 0.4$ cm the temperature starts to increase

sharply, reaching a maximum temperature, $T_{max} = 2240$ K at $z \sim 0.15$ cm. This high temperature region is subsequently referred to as the combustion zone. As decomposition of TTIP releases the gaseous fuel isopropane, C_3H_6, T_{max} increases with increasing TTIP loading (around 100 K difference between 10 and 1070 ppm). Near the stagnation surface, the profile shows a rapid decrease in the temperature as a result of heat loss to the plate.

The axial velocity in Fig. 2(a) is the total of the convective and thermophoretic velocities. The axial velocity initially decreases to 113 cm/s at $z = 0.4$ cm due to flow divergence. At the edge of the combustion zone, the axial velocity increases sharply as a result of strong gas expansion. It is noted that at the stagnation surface, the axial velocity is not zero (≈ 23 cm/s), corresponding to the thermophoretic velocity.

Figure 2(b) shows the evolution of particle size moments in the combustion zone. Before the combustion zone, the moments are virtually constant showing little to no particle processes occuring. The sharp increase in all particle moments, M_0–M_5 shows the formation of particles inside the combustion zone. Initially, all moments are similar in magnitude which indicates nucleation of TiO_2 monomers. As the surface growth and coagulation rates increase, the higher order moments increase more sharply compared to the lower order moments. Near the stagnation surface, the higher order moments increase while the zeroth order moment, M_0, decreases slightly. This is a characteristic of coagulation.

Similar to the particle moments, Fig. 2(b) shows that the TTIP mole fraction is constant before the combustion zone. The TTIP mole fraction decreases in the combustion zone as it is consumed by inception and surface growth. Close to the stagnation surface ($z < 0.1$ cm), the TTIP mole fraction approaches zero, showing that TTIP is almost completely converted to TiO_2 in this region. This is expected considering the high temperature in the combustion zone.

4.1 Comparison with experimental data

4.1.1 Flame location

In the experimental study by Tolmachoff et al. [35], the distance between the stagnation surface and the nozzle, L, is 3.4 cm and the nozzle exit diameter, d, is 1 cm. This corresponds to an L/d ratio of 3.4. This high L/d ratio is an important parameter to consider because ideal one-dimensional stagnation flow equations assume an infinitely wide nozzle exit diameter ($L/d \approx 0$). As a result of the high L/d ratio, a free-jet region with constant velocity is formed upstream of the flame. This free-jet region is not captured by the parabolic solution of the one-dimensional stagnation flow model [4, 5].

The best solution to this problem is to specify the boundary conditions downstream of the free-jet region where the flow is described by the one-dimensional stagnation flow [4]. However, this would require knowledge of the full velocity profile which could only be determined experimentally or with rigorous fluid dynamics simulation.

An alternative solution is to fit the predicted temperature profile to the experimental measurement [19, 35]. This is done by specifying a computational distance, H, that excludes the free-jet region (e.g. $H < L$). In other words, the one-dimensional stagnation flow be-

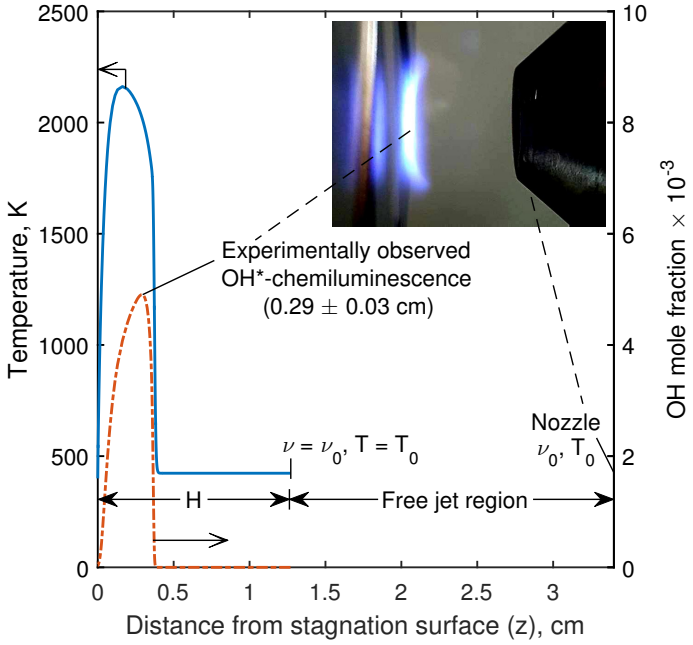

Figure 3: *Simulated temperature and OH*-mole fraction profiles showing the free-jet region upstream of the flame. The inset shows a low exposure image of the flat flame stabilized very near to the stagnation surface (in-house FSRS experiment) for illustration purposes.*

haviour is assumed to start at the end of the free-jet region. Nevertheless, this approach requires an accurate temperature profile which is not available due to the large uncertainty in the current temperature data [35].

In this work, information about the flame location was used to determine the computational distance, H. It was assumed that OH*-chemiluminescence is responsible for the experimentally observed luminosity of the flame. This is a reasonable assumption given that the non-sooting, lean flame was used where particle radiation could be neglected. The peak luminosity was observed at 0.29 ± 0.03 cm [35]. The distance $H = 1.27$ cm was chosen such that the location of the OH* peak predicted by the model coincided with the observed peak luminosity (see Fig. 3). The width of combustion zone is predicted to be slightly less than 0.4 cm which is consistent with experimental observation.

Without taking into account the existence of the free-jet region, the calculation of one-dimensional stagnation flame with $H = 3.4$ cm would result in the flame located almost 1 cm away from the stagnation surface. This is significantly different from the experimental observation and leads to much higher particle residence time in the combustion zone. $T_{\max}$ is also higher due to less heat loss to the stagnation plate.

4.1.2 Particle size and GSD

Tolmachoff et al. [35] showed that the particle size distributions follow a log-normal distribution for all TTIP loadings considered. The fitted particle size distribution was described by its median particle size, $\langle D_p \rangle$, and geometric standard deviation, GSD. In the current

study, the parameters $\langle D_p \rangle$ and GSD were calculated using the following relations,

$$\langle D_p \rangle = \frac{D_p}{\sqrt{1+\frac{\sigma^2}{D_p^2}}} \tag{36}$$

$$\mathrm{GSD} = \exp\sqrt{\log\left(1+\frac{\sigma^2}{D_p^2}\right)}, \tag{37}$$

where D_p and σ are the mean and the standard deviation of the particle size distribution calculated from the reduced particle moments, respectively,

$$D_p = d_1 \mu_{\frac{1}{3}} \tag{38}$$

$$\sigma = d_1 \sqrt{\mu_{\frac{2}{3}} - \mu_{\frac{1}{3}}^2}. \tag{39}$$

Before comparing the model prediction to the experimental data, it is important to consider two aspects of experimental work in Tolmachoff et al. [35], namely stagnation temperature and particle sampling techniques.

In the experiment, the stagnation plate was cooled by a combination of forced convection as a result of the plate rotation and four equally spaced cold jets placed at the back of the stagnation plate. With a total cooling jet volumetric flow of 40 L/min, the stagnation plate temperature, T_s, was shown to be stabilized at ~ 400 K for rotational speeds in the range 100–600 rpm. Without rotation (e.g. 0 rpm), the absence of convective cooling led to T_s reaching as high as $\sim$1000 K although precise measurement was not reported.

Other than the difference in T_s, the experiments with and without rotation also employed different particle sampling techniques. A scanning mobility particle sizer (SMPS) was used for the non-rotating stagnation plate. The sampling probe was mounted inside the plate. This means that the particles were sampled at the stagnation surface (sampling location, $z_{\mathrm{sl}} = 0$). On the other hand, transmission electron microscopy (TEM) analysis with rapid insertion probe was used for the rotating cases. Presumably, the insertion probe samples the particles near the stagnation surface, but not exactly at $z_{\mathrm{sl}} = 0$.

Figure 4 shows the simulated particle size and the geometric standard deviation as functions of TTIP loading and stagnation temperature, T_s. The experimental data is also included for comparison. Figure 4(a) predicts increasing particle size with increasing TTIP loading which is in agreement with experimental data. The particle size is predicted to be a function of T_s, especially for higher TTIP loading at $z_{\mathrm{sl}} = 0$.

Taking into account the lack of convective cooling, the simulated particle size at the stagnation plate ($z = 0$ cm) with $T_s = 1000$ K shows a good agreement with experimental data at 0 rpm. For ease of comparison, the simulated and experimental $\langle D_p \rangle$ and GSD for the five TTIP loadings tested are also presented in Table 1. Without the knowledge of the experimental data uncertainty, however, the significance of the slight under-prediction of the model is difficult to determine.

In order to simulate the effect of rotating stagnation plate, the predicted particle size with $T_s = 400$ K is shown in Fig. 4(a). Compared to $T_s = 1000$ K, the particle size decreases but it does not seem to be enough to explain the significant decrease in the measured particle

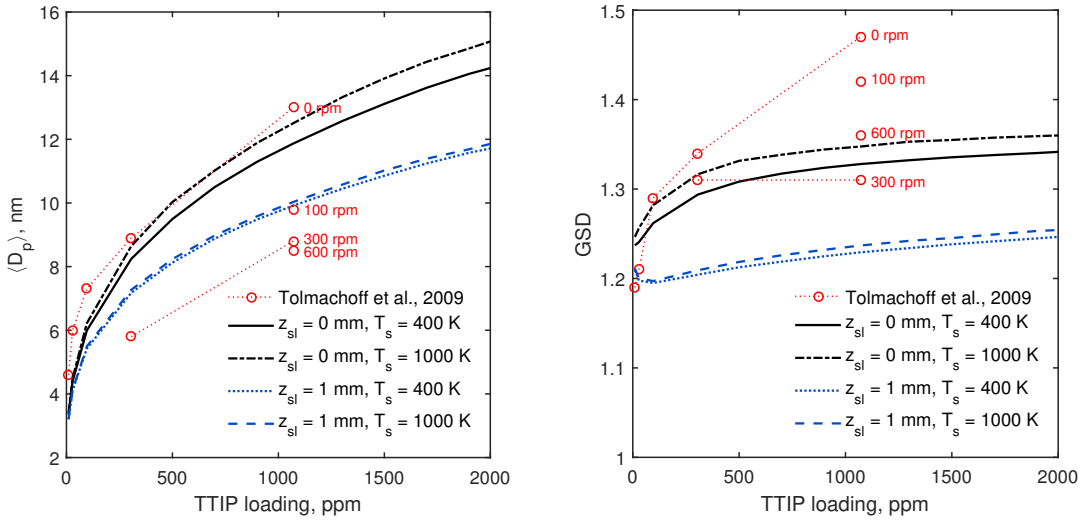

(a) log-Normal median particle size, $\langle D_p \rangle$.

(b) log-Normal geometric standard deviation, GSD.

Figure 4: *Comparison of simulated results and experimental data [35] as function of TTIP loading, T_s, and sampling location from stagnation surface, z_{sl}.*

Table 1: *Simulated and experimental median size, $\langle D_p \rangle$, and geometric standard deviation, GSD, assuming $T_s = 1000$ K. (experimental data is taken from Tolmachoff et al. [35])*

TTIP	Experimental data		Simulation result	
(ppm)	$\langle D_p \rangle$, nm	GSD	$\langle D_p \rangle$, nm	GSD
10	4.6	1.19	3.4	1.25
29	6.0	1.21	4.5	1.26
96	7.3	1.29	6.2	1.28
306	8.9	1.34	8.6	1.32
1070	13.0	1.47	12.5	1.35

size for 100–600 rpm cases. This significant difference could be caused by the difference in sampling techniques. While it has been shown that SMPS and TEM sampling should essentially yield good agreement in particle size measurement [50], the difference in the actual sampling position could lead to a difference in the measured particle size.

An arbitrary distance of $z_{\mathrm{sl}} = 1$ mm was assumed in this work to illustrate the difference of sampling the particles at the surface and near the surface. Figure 4(a) shows the predicted particle size sampled at 1 mm from the stagnation surface. The difference between sampling at 0 and 1 mm is more significant than decreasing T_s. This shows that spatial difference in sampling location of TEM and SMPS could be a potential explanation for the difference in the experimentally observed particle sizes for the rotating and non-rotating case.

Figure 4(b) presents the comparison between the model prediction and experiment for

the geometric standard deviation, GSD. It shows that the GSD increases with TTIP loading, both in the model prediction and the experiment. As the TTIP loading is increased, however, the predicted GSD increases less than the experimental data. The significance of this discrepancy is arguably small considering the uncertainty of GSD measurement (note the scattering in 100–600 rpm data, all at $T_s \sim 400$ K). It is shown that for all TTIP loading in the 0-2000 ppm range, the predicted GSD is smaller than $\sim$1.45, the GSD of a self-preserving size distribution [21] which indicates that coagulation is limited.

Finally, Figure 5 presents the comparison of the log normal density functions for measured and simulated distribution. It shows a good agreement with slight differences in the distribution width and the median particle size.

Some other factors could also affect the interpretation of experimental data. For example, the effects of rotating plate on stagnation flow and boundary layer thickness and the finite flow in SMPS probe [29]. At this stage, the extent of these effects remain as open questions.

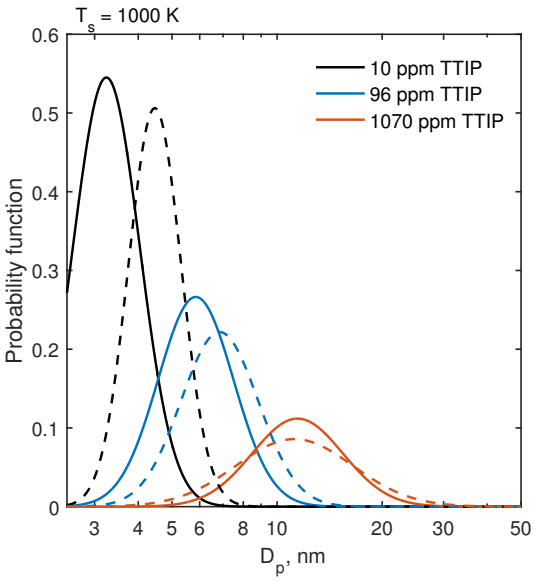

Figure 5: *Log-Normal probability functions for model prediction (solid lines) and experimental data (dashed lines) for varying TTIP loading. The large apparent shift in low TTIP loading case is caused by the log-scaling of the x-axis.*

4.2 Effects of process parameters

4.2.1 Precursor loading

Figure 6(a) shows the simulated temperature profiles as a function of the TTIP loading. Increasing TTIP loading from 10 to 1070 ppm increases $T_{\max}$ from 2130 K to 2240 K due to the release of C_3H_6. Thus, a slight increase in the thermophoretic velocity near the stagnation surface is observed. The combustion zone and OH* profile are slightly broadened, which results in small shifts in the initial temperature increase and OH* peak

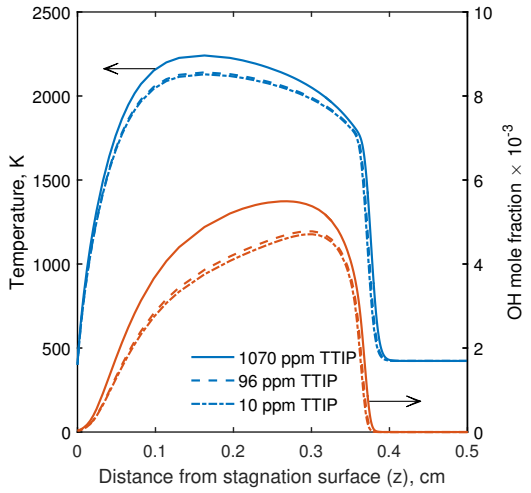

(a) Temperature and OH* mole fraction profiles.

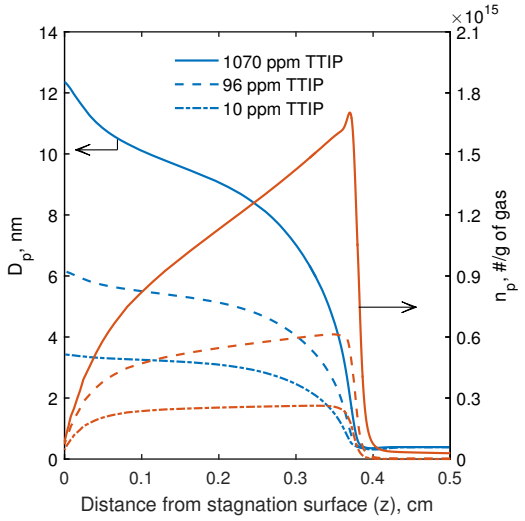

(b) Mean particle size, D_p, and particle number concentration, n_p, evolution along the flame.

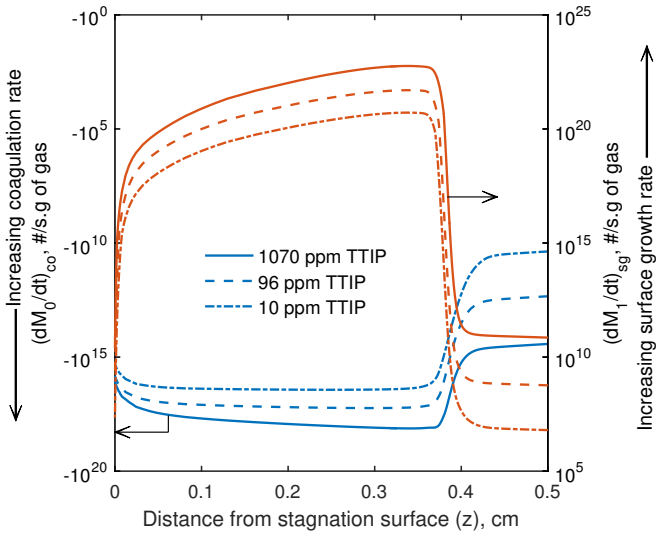

(c) Steady-state source terms for M_0 due to coagulation and M_1 due to surface growth.

Figure 6: *Simulation results with varying precursor loading (10, 96, 1070 ppm TTIP).*

locations. The shift in the OH* peak location is from 0.27 to 0.3 cm.

The mean particle size, D_p, and particle number concentration, n_p, are plotted in Figure 6(b). The number concentration, n_p, was normalized by the gas density, ρ_{gas}, to remove the effect of volume expansion. Initially n_p increases sharply due to inception of TiO_2 monomers, especially for high TTIP loading. This is followed by a gradual decrease for high TTIP loading while almost constant n_p for low TTIP loading. For all cases, D_p increases most sharply at the upstream edge of the combustion zone and also near the stagnation surface.

Figure 6(c) compares the coagulation and surface growth rates in the combustion zone.

Similar to n_p, the rates were also normalized with ρ_{gas}. Note that the coagulation rate has the opposite sign to $\mathrm{d}M_0/\mathrm{d}t$ because M_0 is decreased by coagulation. As temperature increases rapidly in the combustion zone, both surface growth and coagulation rates increase sharply (note the log-scale) because of the high concentration of TiO_2 monomers. As expected, the rates increase with increasing TTIP loading. In this region, the surface growth rate is a few order of magnitude higher than the coagulation rate. This indicates that surface growth is important in the initial stage of particle growth.

As the particles flow downstream ($z = 0.05 - 0.35$ cm), the coagulation and surface growth rates decrease due to the consumption of TiO_2 monomers and TTIP. This is also shown by the steady decrease of n_p and slower increase in D_p in Fig. 6(b).

Near the stagnation surface ($z < 0.05$ cm), both surface growth and coagulation start to decrease more sharply due to the steep decrease in temperature. However, the surface growth rate decreases much faster than the coagulation rate (e.g. surface growth rate drops from 10^{20} to 10^{10} while coagulation rate drops from 10^{17} to 10^{16} /s.g of gas for 1070 ppm loading). Therefore, coagulation is more dominant compared to surface growth in this region which explains the apparent faster increase in D_p and decrease in n_p.

The coagulation-dominated growth leads to the sensitivity of particle size to the sampling location near the stagnation surface. This sensitivity might explain the experimental observation discussed earlier. In addition, the sensitivity is shown to be more pronounced with higher TTIP loading.

4.2.2 Stagnation temperature, T_s

In order to evaluate the effect of the stagnation temperature, the cases with $T_s = 400$, 1000, and 1600 K were simulated for 1070 ppm TTIP loading. The results are shown in Figure 7.

Figure 7(a) shows that increasing T_s broadens the temperature and OH* profiles and significantly reduces the temperature gradient near the stagnation surface. T_{max} increases slightly (2241 K for $T_s = 400$ K, 2260 K for $T_s = 1600$ K) due to less heat loss to the plate. The location of OH* peak shifts slightly from $z = 0.27$ to 0.28 cm (for $T = 400$ and 1600 K, respectively).

As described previously, nucleation initially dominates at the start of the combustion zone, followed by surface growth and coagulation. Figure 7(b) shows a slight shift in the start of the combustion zone. This leads to an earlier increase (and subsequent decrease) of n_p for higher T_s. Thus, at $z \sim 0.1$ cm, n_p is lowest for $T_s = 1600$ K (also for coagulation rate in Fig. 7(c)).

Near the stagnation surface ($z < 0.1$ cm), there is a sharper decrease in n_p (and increase in D_p) for higher T_s. This indicates that coagulation is more dominant in this region for higher T_s despite the lower coagulation rate as shown in Figure 7(c). This is explained by examining the particle time history near the stagnation surface, calculated from the total of convective and thermophoretic velocity. Higher T_s leads to smaller thermophoretic velocity and consequently, higher residence time near the stagnation surface. As a result, the spatial sensitivity of the particle size is expected to be larger for higher T_s. A similar

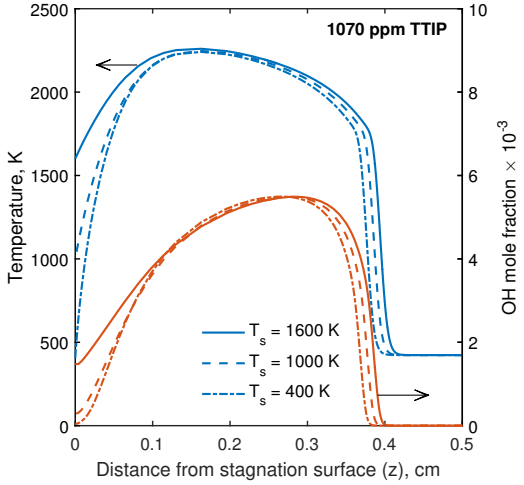

(a) Temperature and OH* mole fraction profiles.

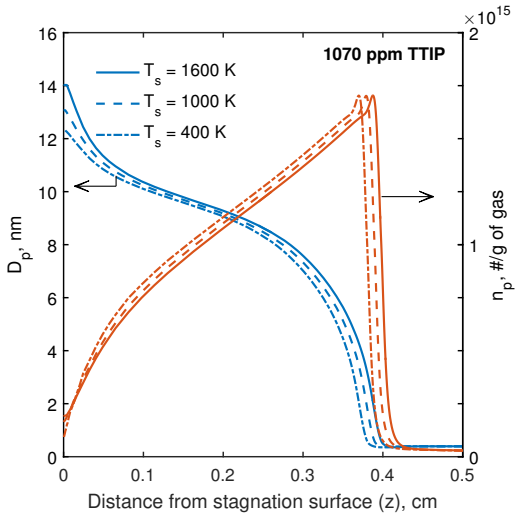

(b) Mean particle size, D_p, and particle number concentration, n_p, evolution along the flame.

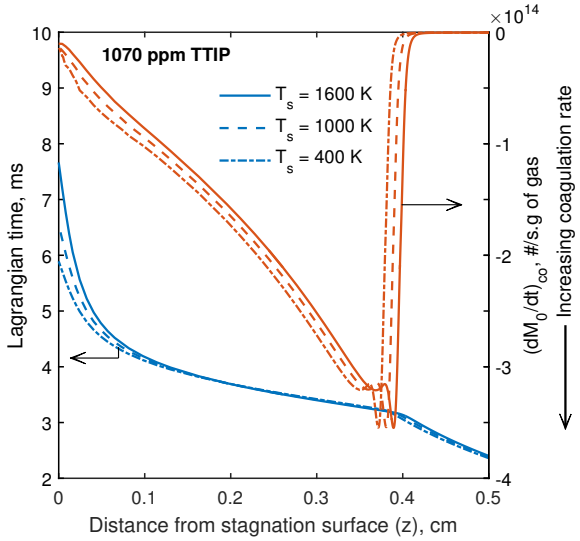

(c) Steady-state source terms for M_0 due to coagulation and calculated Lagrangian particle time.

Figure 7: *Simulation results with varying stagnation temperature, T_s (400, 1000, and 1600 K).*

trend is also observed for smaller TTIP loading.

4.3 Role of surface growth

So far, it has been demonstrated that coagulation plays an important role in the post flame region near the stagnation surface. In this section, the role of surface growth is evaluated by comparing the reaction model described in section 2.3.1 with a reaction model that assumes no surface growth [24]. Without surface growth, the nucleation rate is equal to

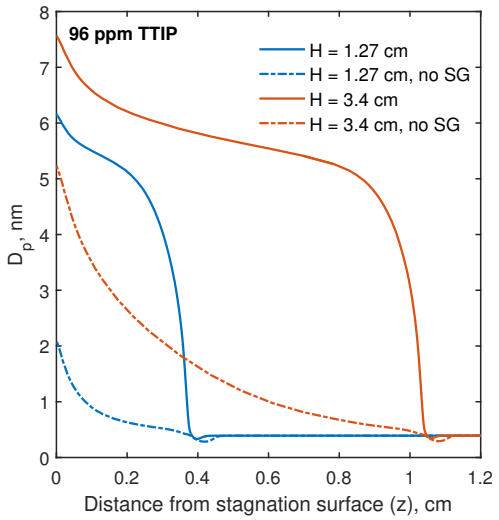

(a) Mean particle size, D_p, evolution along the flame.

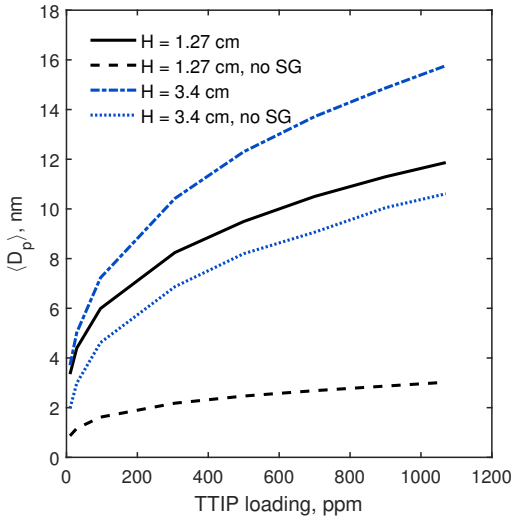

(b) Mean particle size, D_p, at the stagnation surface as function of TTIP loading.

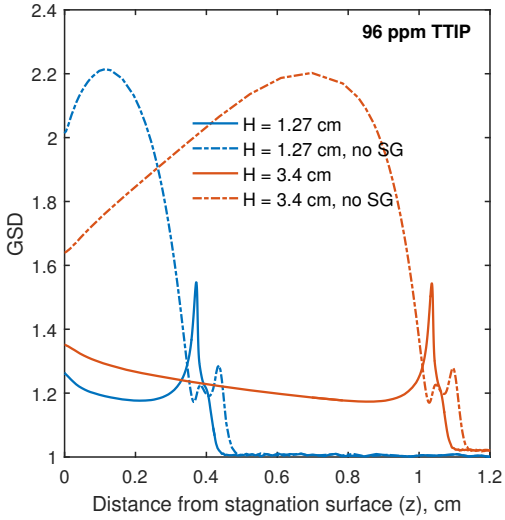

(c) Geometric standard deviation, GSD, evolution along the flame.

Figure 8: *Simulation results with and without surface growth with nozzle-stagnation surface separation distance, H, of 1.27 and 3.4 cm.*

the overall TTIP decomposition rate. Note that in both models, the gas-phase composition and temperature profile are identical because of the equal rate of C_3H_6 release governed by the overall reaction rate.

Figure 8(a) presents the particle size evolution along the flame for both models (with 96 ppm TTIP loading, $T_s = 400$ K). It shows that without surface growth, the particle size is significantly smaller at all locations in the combustion zone. The most important difference is in the initial growth region at the upstream edge of the combustion zone, which shows a more gradual increase of D_p without surface growth compared to the steep increase of D_p with surface growth. This highlights the important role of the surface

reaction in the initial growth stage.

Eventually, the slower growth of the particles at the upstream edge of combustion zone leads to an under-prediction of the particle size at the stagnation surface ($z = 0$). Figure 8(b) shows the sampled particle size at $z = 0$ with and without surface growth for different TTIP loading, showing similar trend for all loadings considered in this work.

In addition, the GSD profiles simulated in Fig. 8(c) indicates significantly broader particle size distribution functions, PSDFs, (with GSD > 1.5) when surface growth is neglected. This is inconsistent with the experimental observation [35].

The original simulations using the model without surface growth [24] appears to yield a good agreement with experimental data. However, the simulations were performed without correcting the computational distance related to the free-jet region. As discussed earlier in section 4.1.1, simulation with $H = 3.4$ cm leads to significantly wider combustion zone. As a result, the slower particle growth is compensated by the longer particle residence time.

It is noted that the importance of surface reaction in the initial particle growth stage has been predicted in the study by Tsantilis et al. [39] (for a premixed flat burner). However, particle sampling close to the flat burner face (< 0.5 cm), where particles are newly incepted, was not feasible. In contrast, a stagnation burner configuration allows experimental investigation of the initial particle growth stage where the masking effect of coagulation is minimized. This results in a high sensitivity to surface growth. Hence, the FSRS setup is a good candidate to investigate TTIP decomposition kinetics and test more detailed TTIP decomposition models.

5 Conclusions

A population balance model describing TiO_2 formation in a stagnation flame reactor was developed by assuming a simple one-step TTIP decomposition reaction. In order to compare the simulation results with experimental data, it is important to account for the existence of the free-jet region in the flow. In this case, the location of the simulated OH* peak was matched with the experimentally observed flame location to estimate the length of the free-jet region.

The simulation results were observed to successfully reproduce the particle sizes measured in the experiment as functions of TTIP loading and stagnation temperature. It was observed that the average particle size and standard deviation increase with increasing TTIP loading and stagnation temperature.

Coagulation was shown to be a dominant process near the stagnation surface. This leads to a high spatial sensitivity of the particle size to the sampling location. The sensitivity increases with increasing TTIP loading and stagnation temperature because of the reduced thermophoretic velocity at the stagnation surface under these conditions. This spatial sensitivity offers a potential explanation for the difference in particle size observed with different experimental sampling techniques. Consequently, it is important to determine the exact experimental sampling location in order to facilitate a direct comparison between

the measured and simulated results.

Further, surface growth was found to play an important role during the initial particle growth at the leading edge of the flame. With decreasing length of combustion zone, surface growth becomes increasingly more important than coagulation in overall. This leads to formation of particles with narrow size distribution and high sensitivity to surface growth. These characteristics make the stagnation flame reactor an attractive experimental tool to validate and improve on the scarce kinetic data available in literature on TTIP decomposition.

6 Acknowledgements

This project is supported by the National Research Foundation (NRF), Prime Minister's Office, Singapore under its Campus for Research Excellence and Technological Enterprise (CREATE) programme. The authors also thank CMCL Innovations for generous financial support.

References

[1] J. Akroyd, A. J. Smith, R. A. Shirley, L. R. McGlashan, and M. Kraft. A coupled CFD-population balance approach for nanoparticle synthesis in turbulent reacting flows. *Chemical Engineering Science*, 66(17):3792–3805, 2011. doi:10.1016/j.ces.2011.05.006.

[2] R. S. Barlow, A. N. Karpetis, J. H. Frank, and J. Y. Chen. Scalar profiles and NO formation in laminar opposed-flow partially premixed methane/air flames. *Combustion and Flame*, 127(3):2102–2118, 2001. doi:10.1016/S0010-2180(01)00313-3.

[3] G. A. Battiston, R. Gerbasi, M. Porchia, and A. Gasparotto. Metal organic CVD of nanostructured composite TiO_2-Pt thin films : A kinetic approach. *Chemical Vapor Deposition*, 5(1):13–20, 1999. doi:10.1002/(SICI)1521-3862(199901)5:1<13::AID-CVDE13>3.0.CO;2-%23.

[4] J. M. Bergthorson, K. Sone, T. W. Mattner, P. E. Dimotakis, D. G. Goodwin, and D. I. Meiron. Impinging laminar jets at moderate Reynolds numbers and separation distances. *Physical Review E*, 72(6):066307, 2005. doi:10.1103/PhysRevE.72.066307.

[5] J. M. Bergthorson, S. D. Salusbury, and P. E. Dimotakis. Experiments and modelling of premixed laminar stagnation flame hydrodynamics. *Journal of Fluid Mechanics*, 681:340–369, 2011. doi:DOI 10.1017/jfm.2011.203.

[6] P. Buerger, D. Nurkowski, J. Akroyd, S. Mosbach, and M. Kraft. First-principles thermochemistry for the thermal decomposition of titanium tetraisopropoxide. *Journal of Physical Chemistry A*, 119(30):8376–8387, 2015. doi:10.1021/acs.jpca.5b01721.

[7] P. Buerger, D. Nurkowski, J. Akroyd, and M. Kraft. A kinetic mechanism for the thermal decomposition of titanium tetraisopropoxide. *Accepted for publication in Proceeding of Combustion Institute*, 2016.

[8] J. Camacho, C. Liu, C. Gu, H. Lin, Z. Huang, Q. Tang, X. You, C. Saggese, Y. Li, H. Jung, L. Deng, I. Wlokas, and H. Wang. Mobility size and mass of nascent soot particles in a benchmark premixed ethylene flame. *Combustion and Flame*, 162(10): 3810–3822, 2015. doi:10.1016/j.combustflame.2015.07.018.

[9] Chemical-kinetic mechanisms for combustion applications, San Diego mechanism web page, Mechanical and Aerospace Engineering (combustion research), University of California at San Diego. URL `http://combustion.ucsd.edu`. Accessed on 4 January 2016.

[10] CMCL Innovations. *k*inetics®, 2016. URL `http://www.cmclinnovations.com/`.

[11] M. Frenklach. Method of moments with interpolative closure. *Chemical Engineering Science*, 57(12):2229–2239, 2002. doi:10.1016/S0009-2509(02)00113-6.

[12] M. Frenklach and S. J. Harris. Aerosol dynamics modeling using the method of moments. *Journal of Colloid and Interface Science*, 118(1):252–261, 1987. doi:10.1016/0021-9797(87)90454-1.

[13] S. Friedlander. *Smoke, dust, and haze: Fundamentals of aerosol behavior*. Topicals in chemical engineering. Wiley, 1977.

[14] J. F. Grcar. The Twopnt program for boundary value problems. Technical Report SAND91-8230, Sandia National Laboratories, 1992.

[15] D. Grosschmidt, H. Bockhorn, M. Goodson, and M. Kraft. Two approaches to the simulation of silica particle synthesis. *Proceedings of the Combustion Institute*, 29 (1):1039–1046, 2002. doi:10.1016/S1540-7489(02)80131-6.

[16] S. J. Harris and I. M. Kennedy. The coagulation of soot particles with van der Waals forces. *Combustion Science and Technology*, 59(4-6):443–454, 1988. doi:10.1080/00102208808947110.

[17] H. M. Hulburt and S. Katz. Some problems in particle technology. *Chemical Engineering Science*, 19(8):555–574, 1964. doi:10.1016/0009-2509(64)85047-8.

[18] R. J. Kee, J. A. Miller, G. H. Evans, and G. Dixon-Lewis. A computational model of the structure and extinction of strained, opposed flow, premixed methane-air flames. *Symposium (International) on Combustion*, 22(1):1479–1494, 1989. doi:10.1016/S0082-0784(89)80158-4.

[19] O. P. Korobeinichev, A. G. Shmakov, R. A. Maksyutov, A. G. Tereshchenko, D. A. Knyazkov, T. A. Bolshova, M. L. Kosinova, V. S. Sulyaeva, and J. S. Wu. Synthesis of mesoporous nanocrystalline TiO_2 films in a premixed H_2/O_2/Ar flame. *Combustion, Explosion, and Shock Waves*, 48(1):49–56, 2012. doi:10.1134/S0010508212010078.

[20] M. Kraft. Modelling of particulate processes. *KONA Powder and Particle Journal*, 23(March):18–35, 2005. doi:10.14356/kona.2005007.

[21] F. S. Lai, S. K. Friedlander, J. Pich, and G. M. Hidy. The self-preserving particle size distribution for Brownian coagulation in the free-molecule regime. *Journal of Colloid and Interface Science*, 39(2):395–405, 1972. doi:10.1016/0021-9797(72)90034-3.

[22] S. Memarzadeh, E. D. Tolmachoff, D. J. Phares, and H. Wang. Properties of nanocrystalline TiO_2 synthesized in premixed flames stabilized on a rotating surface. *Proceedings of the Combustion Institute*, 33(2):1917–1924, 2011. doi:10.1016/j.proci.2010.05.065.

[23] W. J. Menz and M. Kraft. The suitability of particle models in capturing aggregate structure and polydispersity. *Aerosol Science and Technology*, 47(7):734–745, 2013. doi:10.1080/02786826.2013.788244.

[24] A. Modak, K. Puduppakkam, C. Naik, and E. Meeks. Simulation of particle synthesis by premixed laminar stagnation flames. *Materials Research Society Symposium Proceeding*, 1506, 2013. doi:10.1557/opl.2013.1049.

[25] N. M. Morgan, R. I. A. Patterson, and M. Kraft. Modes of neck growth in nanoparticle aggregates. *Combustion and Flame*, 152(1-2):272–275, 2008. doi:10.1016/j.combustflame.2007.08.007.

[26] S. Nikraz and H. Wang. Dye sensitized solar cells prepared by flames stabilized on a rotating surface. *Proceedings of the Combustion Institute*, 34(2):2171–2178, 2013. doi:10.1016/j.proci.2012.06.069.

[27] K. Okuyama, R. Ushio, Y. Kousaka, R. C. Flagan, and J. H. Seinfeld. Particle generation in a chemical vapor deposition process with seed particles. *AIChE Journal*, 36(3):409–419, 1990. doi:10.1002/aic.690360310.

[28] S. E. Pratsinis. Simultaneous nucleation condensation and coagulation in aerosol reactors. *Journal of Colloid and Interface Science*, 124(2):416–427, 1988. doi:10.1016/0021-9797(88)90180-4.

[29] C. Saggese, A. Cuoci, A. Frassoldati, S. Ferrario, J. Camacho, H. Wang, and T. Faravelli. Probe effects in soot sampling from a burner-stabilized stagnation flame. *Combustion and Flame*, 167:184–197, 2016. doi:10.1016/j.combustflame.2016.02.013.

[30] R. Shirley, Y. Liu, T. S. Totton, R. H. West, and M. Kraft. First-principles thermochemistry for the combustion of a $TiCl_4$ and $AlCl_3$ mixture. *Journal of Physical Chemistry A*, 113(49):13790–13796, 2009. doi:10.1021/jp905244w.

[31] R. Shirley, W. Phadungsukanan, M. Kraft, J. Downing, N. E. Day, and P. Murray-Rust. First-principles thermochemistry for gas phase species in an industrial rutile chlorinator. *Journal of Physical Chemistry A*, 114(43):11825–11832, 2010. doi:10.1021/jp106795p.

[32] R. Shirley, J. Akroyd, L. A. Miller, O. R. Inderwildi, U. Riedel, and M. Kraft. Theoretical insights into the surface growth of rutile TiO_2. *Combustion and Flame*, 158 (10):1868–1876, 2011. doi:10.1016/j.combustflame.2011.06.007.

[33] A. G. Shmakov, O. P. Korobeinichev, D. A. Knyazkov, A. A. Paletsky, R. A. Maksutov, I. E. Gerasimov, T. A. Bolshova, V. G. Kiselev, and N. P. Gritsan. Combustion chemistry of $Ti(OC_3H_7)_4$ in premixed flat burner-stabilized $H_2/O_2/Ar$ flame at 1 atm. *Proceedings of the Combustion Institute*, 34(1):1143–1149, 2013. doi:10.1016/j.proci.2012.05.081.

[34] R. Siegel. *Thermal radiation heat transfer, fourth edition*. Taylor & Francis, 2001.

[35] E. D. Tolmachoff, A. D. Abid, D. J. Phares, C. S. Campbell, and H. Wang. Synthesis of nano-phase TiO_2 crystalline films over premixed stagnation flames. *Proceedings of the Combustion Institute*, 32 II(2):1839–1845, 2009. doi:10.1016/j.proci.2008.06.052.

[36] E. D. Tolmachoff, S. Memarzadeh, and H. Wang. Nanoporous titania gas sensing films prepared in a premixed stagnation flame. *Journal of Physical Chemistry C*, 115(44):21620–21628, 2011. doi:10.1021/jp206061h.

[37] T. S. Totton, R. Shirley, and M. Kraft. First-principles thermochemistry for the combustion of $TiCl_4$ in a methane flame. *Proceedings of the Combustion Institute*, 33(1):493–500, 2011. doi:10.1016/j.proci.2010.05.011.

[38] S. Tsantilis and S. E. Pratsinis. Narrowing the size distribution of aerosol-made titania by surface growth and coagulation. *Journal of Aerosol Science*, 35(3):405–420, 2004. doi:10.1016/j.jaerosci.2003.09.006.

[39] S. Tsantilis, H. K. Kammler, and S. E. Pratsinis. Population balance modeling of flame synthesis of titania nanoparticles. *Chemical Engineering Science*, 57(12): 2139–2156, 2002. doi:10.1016/S0009-2509(02)00107-0.

[40] U.S. Geological Survey. *Mineral commodity summaries 2016: U.S. Geological Survey*. 2016. doi:10.3133/70140094.

[41] L. Waldmann and K. Schmitt. *Thermophoresis and diffusiophoresis of aerosols*. Academic Press New York, 1966.

[42] H. Wang, X. You, A. V. Joshi, S. G. Davis, A. Laskin, F. Egolfopoulos, and C. K. Law. USC mech version II. High-temperature combustion reaction model of H_2/CO/C_1-C_4 compounds, 2007. URL `http://ignis.usc.edu/USC_Mech_II.htm`. Accessed on 12 December 2015.

[43] Y. Wang, P. Liu, J. Fang, W.-N. Wang, and P. Biswas. Kinetics of sub-2 nm TiO_2 particle formation in an aerosol reactor during thermal decomposition of titanium tetraisopropoxide. *Journal of Nanoparticle Research*, 17(3):147, 2015. doi:10.1007/s11051-015-2964-y.

[44] K. Wegner and S. E. Pratsinis. Nozzle-quenching process for controlled flame synthesis of titania nanoparticles. *AIChE Journal*, 49(7):1667–1675, 2003. doi:10.1002/aic.690490707.

[45] R. H. West, G. J. O. Beran, W. H. Green, and M. Kraft. First-principles thermochemistry for the production of TiO_2 from $TiCl_4$. *Journal of Physical Chemistry A*, 111:3560–3565, 2007. doi:10.1021/jp0661950.

[46] R. H. West, R. A. Shirley, M. Kraft, C. F. Goldsmith, and W. H. Green. A detailed kinetic model for combustion synthesis of titania from $TiCl_4$. *Combustion and Flame*, 156(9):1764–1770, 2009. doi:10.1016/j.combustflame.2009.04.011.

[47] E. K. Yapp, D. Chen, J. Akroyd, S. Mosbach, M. Kraft, J. Camacho, and H. Wang. Numerical simulation and parametric sensitivity study of particle size distributions in a burner-stabilised stagnation flame. *Combustion and Flame*, 162(6):2569–2581, 2015. doi:10.1016/j.combustflame.2015.03.006.

[48] M. Yu, J. Lin, and T. Chan. Numerical simulation of nanoparticle synthesis in diffusion flame reactor. *Powder Technology*, 181(1):9–20, 2008. doi:10.1016/j.powtec.2007.03.037.

[49] Y. Zhang, S. Li, W. Yan, Q. Yao, and S. D. Tse. Role of dipole-dipole interaction on enhancing Brownian coagulation of charge-neutral nanoparticles in the free molecular regime. *Journal of Chemical Physics*, 134(8), 2011. doi:10.1063/1.3555633.

[50] B. Zhao, K. Uchikawa, and H. Wang. A comparative study of nanoparticles in premixed flames by scanning mobility particle sizer, small angle neutron scattering, and transmission electron microscopy. *Proceedings of the Combustion Institute*, 31 I:851–860, 2007. doi:10.1016/j.proci.2006.08.064.

[51] H. Zhao, X. Liu, and S. D. Tse. Effects of pressure and precursor loading in the flame synthesis of titania nanoparticles. *Journal of Aerosol Science*, 40(11):919–937, 2009. doi:10.1016/j.jaerosci.2009.07.004.